



HAL
open science

Cluster membership probabilities from proper motions and multi-wavelength photometric catalogues. I. Method and application to the Pleiades cluster

L. M. Sarro, H. Bouy, A. Berihuete, E. Bertin, E. Moraux, J. Bouvier, J. -C.
Cuillandre, D. Barrado, E. Solano

► **To cite this version:**

L. M. Sarro, H. Bouy, A. Berihuete, E. Bertin, E. Moraux, et al.. Cluster membership probabilities from proper motions and multi-wavelength photometric catalogues. I. Method and application to the Pleiades cluster. *Astronomy and Astrophysics - A&A*, 2014, 563, 10.1051/0004-6361/201322413 . insu-03618600

HAL Id: insu-03618600

<https://insu.hal.science/insu-03618600>

Submitted on 24 Mar 2022

HAL is a multi-disciplinary open access archive for the deposit and dissemination of scientific research documents, whether they are published or not. The documents may come from teaching and research institutions in France or abroad, or from public or private research centers.

L'archive ouverte pluridisciplinaire **HAL**, est destinée au dépôt et à la diffusion de documents scientifiques de niveau recherche, publiés ou non, émanant des établissements d'enseignement et de recherche français ou étrangers, des laboratoires publics ou privés.



Distributed under a Creative Commons Attribution 4.0 International License

Cluster membership probabilities from proper motions and multi-wavelength photometric catalogues

I. Method and application to the Pleiades cluster[★]

L. M. Sarro^{1,★★}, H. Bouy², A. Berihuete³, E. Bertin⁴, E. Moraux⁵, J. Bouvier⁵, J.-C. Cuillandre⁶,
D. Barrado², and E. Solano^{2,★★}

¹ Dpto. de Inteligencia Artificial, ETSI Informática, UNED, Juan del Rosal, 16, 28040 Madrid, Spain
e-mail: lsb@dia.uned.es

² Centro de Astrobiología, depto. de Astrofísica, INTA-CSIC, PO BOX 78, ESAC Campus 28691, Villanueva de la Cañada, Madrid, Spain

³ Dpt. Statistics and Operations Research, University of Cádiz, Campus Universitario Río San Pedro s/n, 11510 Puerto Real, Cádiz, Spain

⁴ Institut d'Astrophysique de Paris, CNRS UMR 7095 and UPMC, 98bis bd Arago, 75014 Paris, France

⁵ UJF-Grenoble 1/CNRS-INSU, Institut de Planétologie et d'Astrophysique de Grenoble (IPAG), UMR 5274, 38041 Grenoble, France

⁶ Canada-France-Hawaii Telescope Corporation, 65-1238 Mamalahoa Highway, Kamuela, HI96743, USA

Received 31 July 2013 / Accepted 21 January 2014

ABSTRACT

Context. With the advent of deep wide surveys, large photometric and astrometric catalogues of literally all nearby clusters and associations have been produced. The unprecedented accuracy and sensitivity of these data sets and their broad spatial, temporal and wavelength coverage make obsolete the classical membership selection methods that were based on a handful of colours and luminosities. We present a new technique designed to take full advantage of the high dimensionality (photometric, astrometric, temporal) of such a survey to derive self-consistent and robust membership probabilities of the Pleiades cluster.

Aims. We aim at developing a methodology to infer membership probabilities to the Pleiades cluster from the DANCe multidimensional astro-photometric data set in a consistent way throughout the entire derivation. The determination of the membership probabilities has to be applicable to censored data and must incorporate the measurement uncertainties into the inference procedure.

Methods. We use Bayes' theorem and a curvilinear forward model for the likelihood of the measurements of cluster members in the colour–magnitude space, to infer posterior membership probabilities. The distribution of the cluster members proper motions and the distribution of contaminants in the full multidimensional astro-photometric space is modelled with a mixture-of-Gaussians likelihood.

Results. We analyse several representation spaces composed of the proper motions plus a subset of the available magnitudes and colour indices. We select two prominent representation spaces composed of variables selected using feature relevance determination techniques based in Random Forests, and analyse the resulting samples of high probability candidates. We consistently find lists of high probability ($p > 0.9975$) candidates with ≈ 1000 sources, 4 to 5 times more than obtained in the most recent astro-photometric studies of the cluster.

Conclusions. Multidimensional data sets require statistically sound multivariate analysis techniques to fully exploit their scientific information content. Proper motions in particular are, as expected, critical for the correct separation of contaminants. The methodology presented here is ready for application in data sets that include more dimensions, such as radial and/or rotational velocities, spectral indices, and variability.

Key words. methods: data analysis – methods: statistical – catalogs – stars: low-mass – open clusters and associations: general

1. Introduction

The analysis of stellar clusters is one of the stepping stones for understanding galactic and stellar formation and evolution. The study of different clusters reveals properties of the probabilistic distribution of initial masses (the initial mass function, IMF) and its dependence on parameters such as metallicity and age. The

evolution of their dynamical scales and properties can help us understand the history of our own Galaxy and its components. But using clusters as one of the building blocks of our knowledge of the nearer Universe requires identifications of the cluster members as completely and accurately as possible. This work is the first in a series where we apply recent developments in statistics to the problem of estimating the cluster membership probabilities for a set of sources. We concentrate on data sets with both proper motions and multiband photometry.

Traditionally, the problem of estimating membership probabilities based on proper motion measurements has been treated with techniques that followed the pioneering work by

* Membership probability catalogs for the DANCe Pleiades data are only available at the CDS via anonymous ftp to

cdsarc.u-strasbg.fr (130.79.128.5) or via <http://cdsarc.u-strasbg.fr/viz-bin/qcat?J/A+A/563/A45>

** Spanish Virtual Observatory.

Vasilevskis et al. (1958) and Sanders (1971). These works modelled the distribution of sources in the vector point diagram (VPD) as the mixture of two bi-variate Gaussian distributions, one for the cluster members and another for the field sources. The cluster distribution was assumed to be circular in both cases because the astrometric uncertainties did not allow for the detailed resolution of the real shape, and in both cases the membership probability is defined as the posterior probability of the class given the data in this simplified model. Both works adopt a Bayesian approach to inferring membership probabilities, only in the sense that they apply Bayes' theorem. With Bayes' theorem, the posterior probability of the unknown parameter C (the class of the source, i.e., member of the cluster or field populations) given the observed data \mathcal{D} is expressed in terms of a model of the probabilistic distribution of sources of each class in the space of the observed data \mathcal{D} , an a priori membership probability to each class, and a normalising constant:

$$p(C|\mathcal{D}) = \frac{p(\mathcal{D}|C) \cdot p(C)}{p(\mathcal{D})}. \quad (1)$$

We use C , a dichotomic random variable, to represent membership to the foreground and background populations (C_1) or to the stellar cluster (C_2). In the following, the subscript i indexes the two populations, and we use C_i as an abbreviation of $C = C_i$.

In Eq. (1), the posterior membership probability (the left-hand side) is expressed in terms of the likelihood ($p(\mathcal{D}|C)$) and the prior probabilities ($p(C)$ and $p(\mathcal{D})$). It is precisely the likelihood that is modelled in these pioneering works as a symmetric Gaussian distribution in \mathcal{D} , the space of proper motions.

Kozhurina-Platais et al. (1995) combined celestial coordinates with proper motions assuming conditional independency to refine their membership probabilities. They followed the conceptual framework set up by the earlier works cited in the previous paragraph, based on the posterior probability density distribution of a bi-variate Gaussian mixture model. Additionally and alternatively, they proposed an improvement of an original procedure introduced in Platais (1991), where the modelling procedure was treated by partitioning the data into moving bins in a data space that comprises celestial coordinates, proper motions, and the B magnitude. Within each bin, the field distribution is assumed to be a flat linear function in the space of proper motions. The membership probability is then derived using Bayes' theorem locally for each target star in each bin, fixing the mean of the Gaussian distribution in the vector point diagram (VPD) and fitting the prior probabilities with the least-squares estimate in a $8\sigma \times 8\sigma$ square (with σ being the fixed standard deviation of the Gaussian distribution). We recall here that the least-squares fit is equivalent to the maximum-likelihood solution under the assumption of independent Gaussian uncertainties with constant standard deviation. Hence the grouping of the data in magnitude bins. This approach (binning in magnitude) became popular in later works (see Lodieu et al. 2012a, for a recent example). This latter alternative in the work by Kozhurina-Platais et al. (1995) presents several disadvantages in our opinion, including the occasional introduction of faint stars or fractions thereof (*sic*) to avoid negative values of the field-star distribution.

An alternative to this parametric modelling of the distribution of cluster and field members in the VPD was proposed by Balaguer-Núñez et al. (2007), who derived kernel-based estimations of the probability density in the VPD space both for field stars alone (in a region assumed free from cluster members) and for the mixed population in the cluster celestial region.

Later works with combined astrometric and spectro-photometric data sets elaborated further on these early works.

Broad-band photometry is usually considered separately from the astrometric measurements, either before or after the astrometric analysis, and as hard selection thresholds in colour–magnitude or colour–colour diagrams (CMD and CCD respectively; see for example Deacon & Hambly 2004 or Balaguer-Núñez et al. 2007). Usually, these thresholds do not incorporate the photometric uncertainties in a way that retains the probabilistic nature of the memberships, and consist of the refinement of the membership list by removing candidates outside certain bands around the cluster main sequence as defined by theoretical evolutionary tracks. These cuts are also applied in other representation sub-spaces such as derived from radial velocity, spectral type, gravity, activity, metallicity, or lithium line measurements.

The aforementioned work by Lodieu et al. (2012a) and the companion articles Lodieu (2013), Boudreault et al. (2012), and Lodieu et al. (2012b), are recent examples of the classical methodology to derive membership lists from astro- and photometric data sets, this time in the same stellar cluster as studied in the current work: the Pleiades. Lodieu et al. (2012a) defined the cluster sequence in the $(Z - J)$ – Z CMD from previously known members; this sequence induces a conservative photometric cut in the original data set that is meant to remove a large part of field sources; finally, an initial list of membership probabilities is derived following an incorrect version¹ of Eq. (1) applied to the VPD representation space. A threshold of $p = 0.6$ results in 947 member candidates.

The methodologies presented thus far do not extend the probabilistic treatment first put forward by Vasilevskis et al. (1958) and Sanders (1971) for the VPD, to extended data sets with photometric or spectrometric measurements. An exception to this is the recent work by Malo et al. (2013) in young stellar kinematic groups, where the authors treat the astrometric and photometric data consistently in a probabilistic framework, albeit assuming that all measurements included in the inference of membership probabilities are independent and uncorrelated. In general, we find that the application of magnitude-dependent hard thresholds in consecutive CMDs has two main drawbacks: it renders the resulting membership probabilities inconsistent across magnitude bins, and produces membership probabilities only for sources with measurements in each and every CMD used for selection.

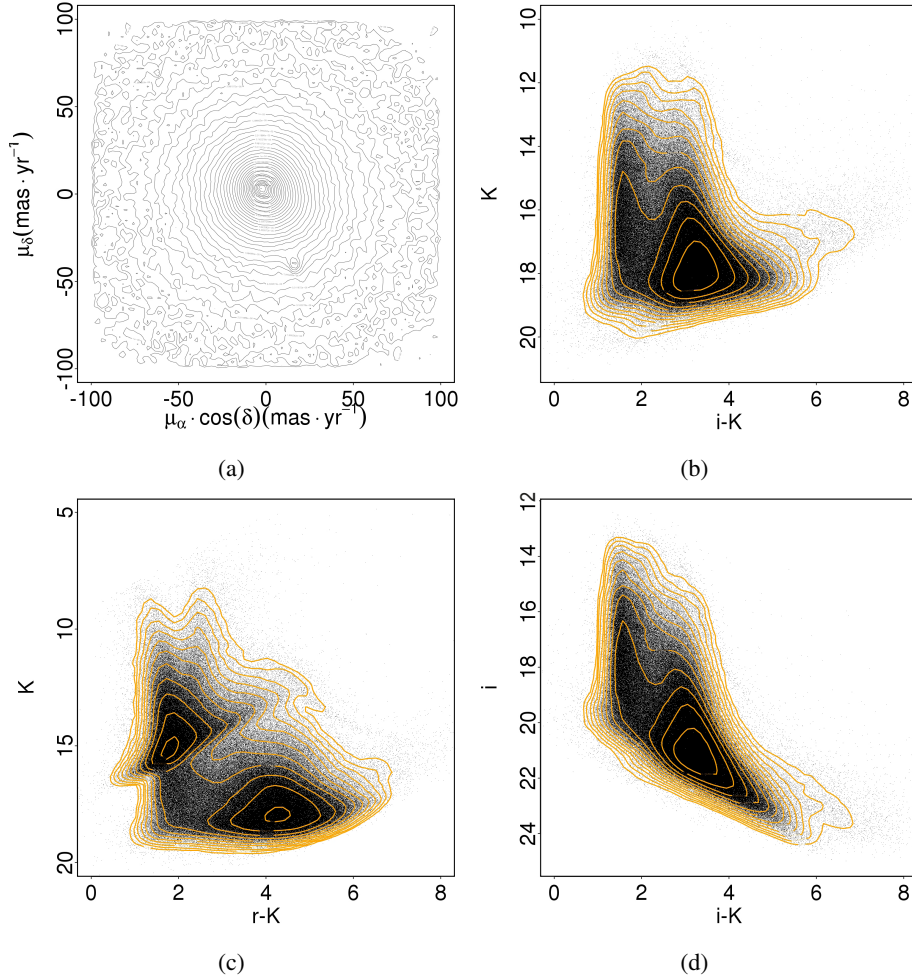
Krone-Martins & Moitinho (2014) have recently developed an unsupervised method for computing membership probabilities from celestial coordinates and photometric measurements using principal components and clustering methods. Their methodology is related to the one presented in this work, and can also incorporate models of uncertainty and incomplete observations. As the authors point out, one of the main disadvantages of their method is the linear projection implicit to the principal components analysis. The distribution of sources in the colour–magnitude space is non-linear in general, and a linear projection inevitably results in membership probabilities that are systematically biased (see Krone-Martins & Moitinho 2014, for a proposal to circumvent this problem).

A final remark on the classical methodology for the determination of membership probabilities in stellar clusters or groups is that the aforementioned works do not incorporate measurement uncertainties into the derivation of the membership probabilities in a consistent way throughout the entire magnitude and proper motion range. We aim at producing membership probabilities

¹ There is a missing factor $(1-f)$ in their Eq. (5). This factor should be multiplying the nominator, and is needed for p to be bounded between 0 and 1, as formally required of a probability.

Table 1. Number of missing measurements.

μ_α	μ_δ	u	g	r	i	Z	Y	J	H	K
0	0	1 842 682	1 627 728	1 294 168	928 902	725 393	724 041	601 758	746 009	768 222

**Fig. 1.** Original DANCe data set for the Pleiades cluster sky region in the VPD **a**), $(i - K)$ – K CMD **b**), $(r - K)$ – K CMD **c**), and $(i - K)$ – i CMD **d**).

with a method that treats astrometric and photometric measurements and their uncertainties consistently. We extend the original probabilistic formulation by Vasilevskis et al. (1958) and Sanders (1971) to include magnitudes and colour indices as part of the representation space where the modelling takes place, and incorporate all the measurement uncertainties (i.e. both astro- and photometric) into the derivation of probabilistic memberships. Another objective of this work is to provide an inference system capable of handling incomplete data (that is, data with non-detections, upper limits, or corrupt values).

In Sect. 2, we describe in more detail the general framework of our methods and the data set that drives the necessity to develop a methodology to infer membership probabilities. In Sect. 3 we discuss the set of random variables used to represent sources in the modelling of the distribution corresponding to the cluster and the field, and alternative spaces tested in the experimentation phase. In Sect. 4 we describe the results obtained with two sets of models, and in Sect. 5 we analyse the sensitivity of these results to the various choices of parameters and representation space. Finally, in Sect. 6 we expose the weaknesses and limitations of this methodology and point out future developments that circumvent these limitations.

2. Membership probability estimation

2.1. Observations

We explore probabilistic models for the estimation of membership probabilities in a multidimensional data set composed of proper motions and apparent magnitudes of sources in the Pleiades cluster sky region. The origin of the data set and the typical uncertainties are described in Bouy et al. (2013). The data set is composed of proper motions in equatorial coordinates (μ_α, μ_δ) and measurements in the $u, g, r, i, Z, Y, J, H,$ and K bands for 3 577 478 sources. From these, we selected 2 066 111 sources with proper motions between $\pm 100 \text{ mas yr}^{-1}$ (hereafter, the DANCe data set). Unfortunately, the data set is inhomogeneous in the various bands, with different spatial coverages, completenesses, and limiting magnitudes (see Fig. 1 in Bouy et al. 2013, for a graphical representation of the complex spatial coverage of the DANCe Pleiades data set).

As a consequence, only 132 067 sources are complete (have photometric measurements in all bands). Table 1 summarises the number of missing measurements in each variable, and Fig. 1 shows the distribution of sources in the proper motion

diagram or VPD (top left) and several colour–magnitude subspaces (K versus $(i - K)$, i versus $(i - K)$, and K versus $(r - K)$, from top right to bottom left clockwise).

We used an initial list of Pleiades candidate members (derived from [Stauffer et al. 2007](#)) as the starting point for the derivation of our models. We will refer to this initial list as the initial reference set.

2.2. Methodology

The approach adopted here consists of inferring the posterior membership probability given the observations \mathcal{D} , $p(C|\mathcal{D})$, using Bayes' theorem (Eq. (1)).

In Eq. (1), the posterior membership probability (the left-hand side) is expressed in terms of the likelihood ($p(D|C)$) and the prior probabilities ($p(C)$ and $p(\mathcal{D})$). We define the prior membership probability as the proportion of cluster members in the entire data set.

In addition to the prior probabilities, a mathematical model of the likelihood is needed to convert prior into posterior probabilities. In the following paragraphs we explain our strategies to derive the likelihood function.

We modelled the distribution of examples of both members and non-members in several representation spaces discussed below. For example, a representation space can be composed of the two proper motions, and a subset of magnitudes and colour indices. These are the variables used to represent each source. In all cases, the likelihood model was derived only from complete observations, that is, from sources that have measurements available for all variables defining the representation space. This likelihood model was then used in Eq. (1) to infer the membership probabilities of all sources in the DANCe Pleiades data set.

We did not include in this likelihood model the spatial distribution of cluster members in the celestial sphere. This is because one of the main objectives of the analysis of the Pleiades DANCe dataset is to infer this spatial distribution and study the statistical significance of potential dependencies on the stellar mass. Thus, we preferred to not assume any model for the cluster members spatial density, and derived membership probabilities only from proper motions and colour–magnitude diagrams. We postpone the inclusion of the spatial information until a detailed analysis of the physical properties of the cluster members is carried out and made public in a future article in this series.

Both the initial list of Pleiades candidate members and the set of DANCe sources in the field are the result of a spatial selection on the celestial sphere and on the VPD diagram. Furthermore, since the likelihood model is only inferred from complete observations, the spatial footprint of the different instruments included in the data set represents yet another source of biases. The selection based on celestial coordinates is defined by a circle of 5 degrees radius around the centre of the cluster; the selection in the VPD is bounded by maximum proper motions in any of the two axes of 100 mas yr^{-1} . This ab initio selection procedure defines the proportion of the two types of sources (field and cluster) and therefore affects the posterior probabilities via the likelihood and prior probability, as indicated in Eq. (1). The posterior probabilities derived in this work are thus not an absolute scale, but are those derived from the actual data set, with the biases inherent to the preparation of the DANCe catalogue.

In Sect. 6 we indicate a rigorous and consistent way to take these selection biases into account; this involves multilevel or hierarchical modelling of the data set.

2.3. Mixture-of-Gaussians model for the field sources

We began by modelling the distribution of foreground and background sources in the representation space with a mixture-of-Gaussians model. The mixture-of-Gaussians model is a simple linear combination of k_1 multivariate normal (Gaussian) distributions, with the index 1 referring to the set of field contaminants (stars mostly, although it may contain one or various types of extragalactic sources, an issue that will be pursued further in future works).

A model is given by the k_1 means ($\mu_{1,j}$, $j = 1, 2, \dots, k_1$) and covariance matrices ($\Sigma_{1,j}$, $j = 1, 2, \dots, k_1$) of the multivariate normal components in the mixture. We denote this set of parameters as θ_1 . Below we use the subscript j for indexing mixture components. Let \mathbf{m} be the vector of observations (the subset of proper motions, apparent magnitudes and colour indices) used to represent sources. Then, the mixture-of-Gaussians model of the likelihood for the field sources is defined as

$$p(\mathbf{m}|C_1) = \sum_{j=1}^{k_1} \pi_{1,j} \cdot \mathcal{N}_{\mu_{1,j}, \Sigma_{1,j}}(\mathbf{m}), \quad (2)$$

with \mathcal{N} representing the normal Gaussian probability density, and $\pi_{1,j}$ the mixture proportions (i.e., the probability that a given source belongs to the mixture component j).

We obtained maximum-likelihood models using the expectation-maximisation (EM) algorithm for a sequence of k_1 values. The EM algorithm is not guaranteed to find the global maximum of the likelihood landscape, but repeated runs with subsamples of the complete data set did not result in large variations, either in the number of components, or in the fitted parameters.

We denote the values of θ_1^k that maximise the likelihood function with k Gaussian components as $\hat{\theta}_1^k$. $\mathcal{L}_{\hat{\theta}_1^k}$ is the maximum likelihood found by the EM algorithm for the family of models defined as a sum of k multivariate normal distributions with full covariance matrices, and the data set defined by n data points (sources) of dimension d . We then selected the likelihood model that maximises the Bayesian information criterion (BIC), given by

$$\mathcal{M} = -2 \ln(\mathcal{L}_{\hat{\theta}_1^k}) + k \frac{d(d+3)}{2} \ln(n). \quad (3)$$

The BIC represents a regularised figure-of-merit with a penalty term for complex models derived in the Bayesian framework for multivariate distributions ([Schwarz 1978](#)).

2.4. Principal curve models for the cluster members

In Sect. 2.3 we modelled the likelihood term in Eq. (1) for the field sources as a sum of multivariate normal distributions. To avoid the overfitting of the data, we used a regularised maximum-likelihood criterion with a penalty for complex models (i.e., the BIC). While this approach is a good starting point for the complex distribution of field sources shown in Fig. 1, for the cluster likelihood model we chose a different class of models in which the probability density of the data in the magnitude–colour subspace of the representation space can be modelled by a curve. In this section, we construct a simplified model of the distribution of cluster members in which the variables pertaining to the proper motions and colour–magnitude subspaces are independent. Therefore, the full likelihood model

is decomposed as the product of two models, one for each subspace. The model for the subspace of proper motions still is a mixture-of-Gaussians, while the likelihood model for the colour–magnitude (CM) subspace is a curvilinear one based on principal curves, as described below. Formally,

$$p(\mathbf{m}|\mathcal{C}_2) = \sum_{j=1}^{k_2} \pi_{2,j} \cdot \mathcal{N}_{\mu_{2,j}, \Sigma_{2,j}}(\mu_\alpha, \mu_\delta) \cdot p(\mathbf{m}_{\text{CM}}|\mathcal{C}_2), \quad (4)$$

where $p(\mathbf{m}_{\text{CM}}|\mathcal{C}_2)$ is the curvilinear likelihood model for the probability density distribution in the CM subspace.

The choice of an empirical curve over a theoretical isochrone frees us from any assumptions on the cluster’s parameters (e.g. age, distance, metallicity) or from the model uncertainties, which are especially important at young ages. We have also tested a single mixture-of-Gaussians model for the sample of sources that belong to the cluster, and the full set of variables pertaining to the proper motion and CM subspaces. However, although normal densities are good approximations to the distribution of data in the space of proper motions, these do not model the distribution in the CMDs satisfactorily. From stellar evolution theory we know that this distribution follows a narrow set of isochrones that can be represented as a multivariate curve in the colour–magnitude subspace. The mixture-of-Gaussians likelihood model requires three components (as assessed by the BIC) to reproduce the curvilinear distribution, and the resulting covariances are too large to accommodate the curvilinear nature of the distribution. This results in conspicuously contaminated membership lists, and therefore we do not describe this set of models further.

We obtained a curvilinear likelihood model by fitting a principal curve (Hastie & Stuetzle 1989) to the list of members. Principal curves analysis is one of the various extensions of principal components analysis to non-linear probability distributions that aims at minimising the sum of square deviations in all variables in representation space. This is accomplished with an iterative scheme whereby the current version of the curve (initially the first principal component) is modified in two steps: projection and conditional expectation. The principal curve is represented by a set of points f_l (with $l = 1, 2, \dots, n$) in representation space that can be interpolated with various models of different degrees of complexity. Given our typical densities, a linear interpolation scheme is more than sufficient. This piecewise linear interpolation defines a parametrisation of the curve that can be thought of as a length along the curve, measured from one of the extremes. We defined $s(\lambda)$ as this parametrisation of the curve.

The projection step finds the point in the curve closest (in the Euclidean sense) to a given observation $\mathbf{m}_{\text{CM},l}$, and assigns a coordinate value λ_l to it. The conditional expectation step redefines the set of points $\{f_l, l = 1, 2, \dots, n\}$ used for interpolation as the expected value of colour–magnitude observations with $\lambda = \lambda_l$:

$$f_l = E(\mathbf{x}_{\text{CM}}|\lambda = \lambda_l), \quad (5)$$

where \mathbf{x}_{CM} is the random variable from which the observations \mathbf{m}_{CM} are drawn.

Since typically each observation projects onto a different value of λ , some kind of smoothing scheme is needed in the expectation step. We used a smoothing spline (see e.g., Hastie & Tibshirani 1990) of df degrees of freedom, where df depends on the representation space. This number of degrees of freedom is the minimum necessary to model the distribution in the various two-dimensional projections without conspicuous biases. Several tests showed that principal curves obtained in a range of degrees of freedom are barely distinguishable from one another

and produce the same candidate lists. When the iterations converged, the same smoothing scheme was used to define the variance $\Sigma(\lambda)$ along the curve.

The final likelihood-model in the CM subspace is defined as

$$p(\mathbf{m}_{\text{CM}}|\mathcal{C}_2) = p(\lambda) \cdot p(\mathbf{m}_{\text{CM}}|\lambda), \quad (6)$$

where $p(\lambda)$ is interpolated from the empirical kernel density estimate of sources per $d\lambda$, and $p(\mathbf{m}_{\text{CM}}|\lambda)$ is modelled with a multivariate normal distribution, the covariance of which is again interpolated from the empirical distribution of covariances estimated from sets of sources within intervals of $\Delta\lambda$. This effectively overestimates the true covariance since the estimated values respond not only to the natural spread of the isochrone, but also to the measurement errors.

We found clear evidence of an isochrone parallel to (and brighter than) the main cluster component. This is interpreted as the result of the presence of equal mass binaries in the cluster sample. In general, the spread of the sequence is due to the combined effects of multiplicity (at all possible luminosity ratios), intrinsic variability, and rotation. We only modelled equal mass binaries with a second likelihood-component identical to the cluster principal curve, but displaced in the magnitude space by 0.75 mag. The relative prior probabilities for the two principal curves were set ad hoc to 0.8 and 0.2 for the main sequence and the sequence of binaries, respectively. These values were not updated during the iterations because the binarity of the sources is not amongst the set of inferred parameters, but also because this fraction varies with stellar luminosity. We checked the consistency of this choice in view of the resulting membership lists in Sect. 5, and discuss alternatives in Sect. 6.

To prevent binaries from biasing the principal curve estimation, we fitted it in two stages. In the first stage, we computed the principal curve for the complete list of members in each iteration of the EM algorithm. This fit is expected to be biased towards brighter magnitudes due to the presence of binaries. We subsequently filtered out sources that are brighter in all magnitudes of the representation space than the closest (in the Euclidean sense) point in the principal curve. We also removed points with Mahalanobis distances from this closest point greater than 15 (a somewhat arbitrary but conservative value that only removes clear outliers). We then recomputed the principal curve with the filtered data set.

Figure 2 shows these two consecutive fits to the initial reference data. The blue line corresponds to the first principal component fit to the initial reference set (with outliers removed), while the green line represents the second fit to the subset represented as red circles.

As mentioned above, we maintain the mixture-of-Gaussians model, and the model complexity selection based on the BIC for the subspace of proper motions of cluster members.

2.5. Iterative refinement of the initial reference set

In the previous paragraphs we have described the derivation of the likelihood models from the initial reference set defined by the membership list in Stauffer et al. (2007). Close examination of the membership probabilities derived from Eq. (1) and these likelihood models reveals the presence of sources in the initial reference set with low membership probabilities and vice versa. Therefore, and for the sake of self-consistency, we adopted an iterative procedure, based again on the EM algorithm, whereby we derived likelihood models in iteration l from the membership lists calculated in iteration $l - 1$ (maximisation step). Then, we

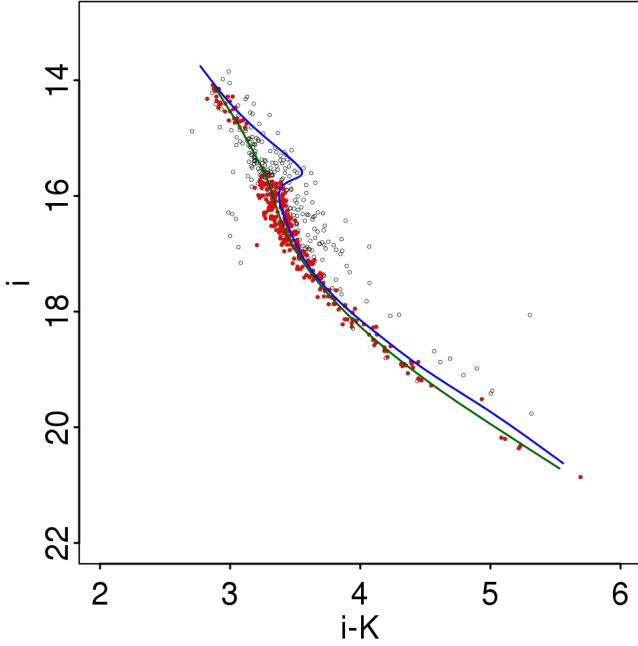


Fig. 2. Principal curve fits to the initial reference set (blue line) and to the subset of sources with all magnitudes fainter than its closest point in the first principal curve (green line). This subset of points is represented in red.

used these likelihood models to infer membership probabilities (expectation step), and proceeded to the next iteration, $l + 1$.

The first iteration proceeded as described in the previous sections, with the data set \mathcal{D} defined by the set of sources observed in all the variables in representation space, and with the class labels C taken from [Stauffer et al. \(2007\)](#). Let $p_0(\mathcal{D}|C_i)$ denote the initial likelihood models derived from the initial reference set. In subsequent iterations, the regularised maximum-likelihood model, together with Eq. (1), were used to infer posterior membership probabilities (expectation step). Since the two models by definition comprise all possibilities, we can compute the posterior probability in iteration l as

$$p_l(C_i|\mathcal{D}) = \frac{p_{l-1}(\mathcal{D}|C_i) \cdot p_{l-1}(C_i)}{\sum_{i=1}^2 p_{l-1}(\mathcal{D}|C_i) \cdot p_{l-1}(C_i)} \quad (7)$$

We took into account the measurement uncertainties in the likelihood term as follows:

$$p_{l-1}(\mathbf{m}_{\text{measured}}|C_i) = \int p_{l-1}(\mathbf{m}|C_i) \cdot p_{l-1}(\mathbf{m}_{\text{measured}}|\mathbf{m}) d\mathbf{m} \quad (8)$$

where $\mathbf{m}_{\text{measured}}$ represents the measured values. We assumed independent Gaussian uncertainties in all measured variables (proper motions and apparent magnitudes) and thus,

$$p_{l-1}(\mathbf{m}_{\text{measured}}|\mathbf{m}) = \mathcal{N}_{\mathbf{m},\Sigma}(\mathbf{m}_{\text{measured}}), \quad (9)$$

where Σ represents the non-diagonal covariance matrix of the variables in representation space. The matrix elements were derived following the usual rules for uncertainty propagation of variables that are linear combinations of the original ones (the colour indices).

We then redefined the membership lists according to these posterior probabilities. We used two heuristic thresholds p_{in} and p_{out} , such that members with posterior membership probabilities below p_{out} were removed from the training set of cluster members, while non-members with posterior membership

probabilities above p_{in} were included in it. We have tested three values of $p_{\text{in}} = \{0.9545, 0.975, 0.9975\}$ (probability values corresponding to the range from 2σ to 3σ significance), and set $p_{\text{out}} = 0.5$. This represents criteria that are very restrictive for the admission of sources not previously classified as members in the literature, while somewhat conservative for the rejection of members.

With these updated membership lists we derived new likelihood models $p_l(\mathcal{D}|C_i)$ and prior probabilities (the maximisation step), and iterated the EM scheme until the membership lists remained unchanged.

We stress that the implicit extrapolation of the principal curve beyond the range of magnitudes and colours covered by the initial reference set, carried out during the EM iterations, is not blind, but constrained to be based on sources with high membership probabilities, and thus is highly consistent with the distribution in the proper motion space.

When the iterations converged to a stable solution (defined by no change in membership for any source in two consecutive iterations), we computed membership probabilities for incomplete sources (i.e., sources with missing data) by again applying Bayes' theorem, with a likelihood model obtained by marginalising the complete maximum-likelihood model derived in the previous section over the missing variables:

$$p(\mathbf{m}_{\text{measured}}|C_i) = \int p(\mathbf{m}|C_i) \cdot d\mathbf{m}_{\text{missing}}, \quad (10)$$

where $\mathbf{m} = \{\mathbf{m}_{\text{measured}}, \mathbf{m}_{\text{missing}}\}$, and $\mathbf{m}_{\text{measured}}$ and $\mathbf{m}_{\text{missing}}$ are the subsets of \mathbf{m} that are measured and missing, respectively. Since the model for $p(\mathbf{m}|C_i)$ is a mixture of Gaussians, the result of the integral is again a mixture of Gaussians with means and covariance matrices that correspond to the projection of the original ones onto the subspace of measured variables. Uncertainties are handled in the same way as described in Eq. (8).

3. Representation space

It is well known that not all variables are equally informative for the determination of membership probabilities. As a matter of fact, apparent magnitudes alone may be insufficient for the selection of member candidates, and it is common practice to define hard boundaries in CMDs (see e.g. [Lodieu et al. 2012a](#)). Including non-informative variables may also dilute the discriminative power of relevant ones, thus leading to poor performances. We explored several representation spaces and assessed their relative merits.

As shown in Table 1, 89% and 79% of the sources do not have measurements in the u and g bands, respectively. We excluded these two bands to avoid creating initial models of the member and field samples composed exclusively of bright, relatively hot objects.

We assessed a number of representation spaces summarised in Table 2.

The first set of variables corresponds to the set of apparent magnitudes; the second set corresponds to the set of colour indices defined by two consecutive spectral bands; the third set corresponds to a heuristic set defined intuitively as relevant for the separation of the two classes; the fourth, fifth, and sixth sets correspond to the heuristic feature set with one apparent magnitude added to it (r , i , and K , respectively); the seventh and eighth feature sets were obtained by performing an importance analysis with random forests (see below for a more detailed explanation) induced from the set of features defined by the heuristic set of

Table 2. Representation spaces evaluated in this work.

Experiment	Representation space
Apparent magnitudes (AM)	$\mu_\alpha \mu_\delta, r, i, J, H, K, Y, Z$
Colour indices 1 (CI-1)	$\mu_\alpha \mu_\delta, (r - i), (i - Z), (Z - Y), (Y - J), (J - H), (H - K)$
Colour indices 2 (CI-2)	$\mu_\alpha \mu_\delta, (i - J), (i - K), (Y - J), (Z - J), (r - H), (r - K)$
$r + \text{CI-2}$	$\mu_\alpha \mu_\delta, r, (i - J), (i - K), (Y - J), (Z - J), (r - H), (r - K)$
$i + \text{CI-2}$	$\mu_\alpha \mu_\delta, i, (i - J), (i - K), (Y - J), (Z - J), (r - H), (r - K)$
$K + \text{CI-2}$	$\mu_\alpha \mu_\delta, K, (i - J), (i - K), (Y - J), (Z - J), (r - H), (r - K)$
RF-1	$\mu_\alpha \mu_\delta, r, J, H, K, (i - J), (r - K)$
RF-2	$\mu_\alpha \mu_\delta, J, H, K, (i - K), (r - K), (Y - J)$
RF-3	$\mu_\alpha \mu_\delta, J, H, K, Y, (i - Z), (r - Y), (r - i)$

colour indices plus the set of apparent magnitudes; finally, the ninth feature set was again derived from an importance analysis with random forests, but induced now from the entire set of apparent magnitudes and all potential colour indices.

The variable sets RF-1 and RF-2 in Table 2 are defined by the most important variables, with importance measured by the mean decrease in accuracy, and by the mean node impurity obtained for out-of-bag (OOB) samples and a random forest classifier (Breiman 2001).

A random forest is a relatively large number of classification trees. A classification tree, in turn, is a tree-like decision graph that predicts the class of an input case (in our context, whether a source belongs to the cluster or field subsets) by successively applying tests on subsets of the representation space variables. The tests on the variables take the form of conjunctions of conditionals, for example, $m_i > \zeta_i$ AND $m_j < \zeta_j$, where ζ acts as a decision boundary, and we omitted the distinction between measured and true values of the variables to simplify notation. These tests are represented as nodes in the tree; each arc connecting nodes represents possible outcomes of the test; and the leaf nodes represent class assignments. Each classification tree in a random forest is constructed using random subsets of representation space variables for the tests performed in each of the tree nodes. A more detailed explanation of the induction algorithm that constructs the tree from a given training set is beyond the scope of this article. Descriptions of the methodology used here can be consulted for instance in Murphy (2012).

The decision boundaries in each node of each tree in the random forest are inferred from bootstrap samples of the initial reference data set, from which a set of examples was separated for testing purposes (the OOB sample). By randomly shuffling the values of a given representation space variable and subsequently quantifying the classification performance degradation, we gauged the relative importance of that variable. We expect that shuffling of the values of irrelevant (non-informative) variables will result in little or no performance degradation. In the case of RF-1 and RF-2, the random forests were induced, as mentioned above, by using a training set comprising all apparent magnitudes and the set of colour indices defined heuristically (CI-2), while RF-3 was defined by the random forest induced from a training set that includes all apparent magnitudes and all potential colour indices. In all cases, proper motions, magnitudes, or colour indices were added in decreasing order of importance (starting from an empty set) until the next variable is a linear combination of the current set of variables. The total number of variables used in the various models is thus limited by the requirement that the covariance matrices in the mixture-of-Gaussians have to be invertible. Proper motions appear selected in the top places of the ranking in all cases.

We visually checked the results (final reference sets and membership probability distributions for the entire DANCe data set) of the algorithms for each representation space in Table 2. In the current work we only show detailed results for three representation spaces (AM, RF-2, and RF-3) selected on the basis of three criteria: higher exhaustivity (we preferred representation spaces that produced isochrones that reached fainter magnitudes), lower contamination rates (we avoided representation spaces that result in conspicuously contaminated membership lists), and conciseness (we did not include representation spaces that produced the same reference set and thus, membership probabilities as one already selected).

4. Results

In this section we discuss the results obtained for the RF-2 representation space and $p_{\text{in}} = 0.975$, for the model described in Sect. 2 (that is, a mixture-of-Gaussians model for the field sources in the full RF-2 representation space, and a mixed model for cluster sources composed of a mixture-of-Gaussians in the proper motions subspace and a curvilinear model in the CM subspace). In Sect. 5 we briefly discuss the sensitivity of these results as we change p_{in} and the representation space. In particular, we compare the results discussed in this section with those obtained for the RF-3 representation space in more detail.

We carried out the iterative scheme described above in two stages. In the first stage we used the full representation space, while the second stage was performed in a reduced subspace without variables (colour indices) derived from the r band. This is because the number of complete sources in the reduced subspace is significantly larger than in the original subspace, as can be deduced from Table 1, especially for the reddest sources.

Since there are in fact known member candidates from the literature that are complete in the reduced feature subspace, but incomplete in the original RF-2 set (that is, members detected in all bands used in the RF-2 set except in the r band), we added these sources to the membership list obtained in the full feature space. This approach has the disadvantage that the lack of constraints for the r magnitude allows including of member candidates far apart from the defining isochrone in the full space if the large distance is only due to discrepancies in that magnitude.

Using the RF-2 representation space, the BIC selected 2 and 26 Gaussian components for the likelihood models of the cluster (proper motion subspace) and field populations, (full RF-2 representation space) respectively.

Figure 3 shows the final reference set of cluster members (complete sources used to define the likelihood model) for this representation space. The contour lines represent the iso-density lines computed using a Gaussian kernel density estimation

Table 3. Mean decrease in accuracy and node impurity of random forests trained with the heuristic set (Cols. 2 and 3) or the complete set (Cols. 5 and 6) of proper motions, magnitudes, and colour indices.

Variable	Heuristic set: mean decrease in classification accuracy	node impurity	Variable	Full set: mean decrease in classification accuracy	node impurity
μ_δ	0.0021	530.6	μ_δ	0.0016	369.6
μ_α	0.0015	199.4	μ_α	0.0010	130.1
$r-K$	0.0014	156.0	K	0.0013	114.8
K	0.0024	127.1	J	0.0016	98.0
$i-K$	0.0008	102.0	H	0.0011	85.7
H	0.0012	80.1	$r-Z$	0.0008	82.0
$Y-J$	0.0006	77.9	Y	0.0014	70.6
J	0.0017	77.3	$r-Y$	0.0007	60.2
$r-H$	0.0005	48.7	$r-H$	0.0006	57.5
Y	0.0009	41.8	$r-J$	0.0006	55.4
$Z-J$	0.0002	27.3	Z	0.0011	47.0
Z	0.0007	21.6	$i-Y$	0.0004	44.5
i	0.0009	18.8	$r-i$	0.0004	43.1
r	0.0011	17.5	$r-K$	0.0004	42.9
$i-J$	0.0013	16.0	$i-Z$	0.0004	36.5

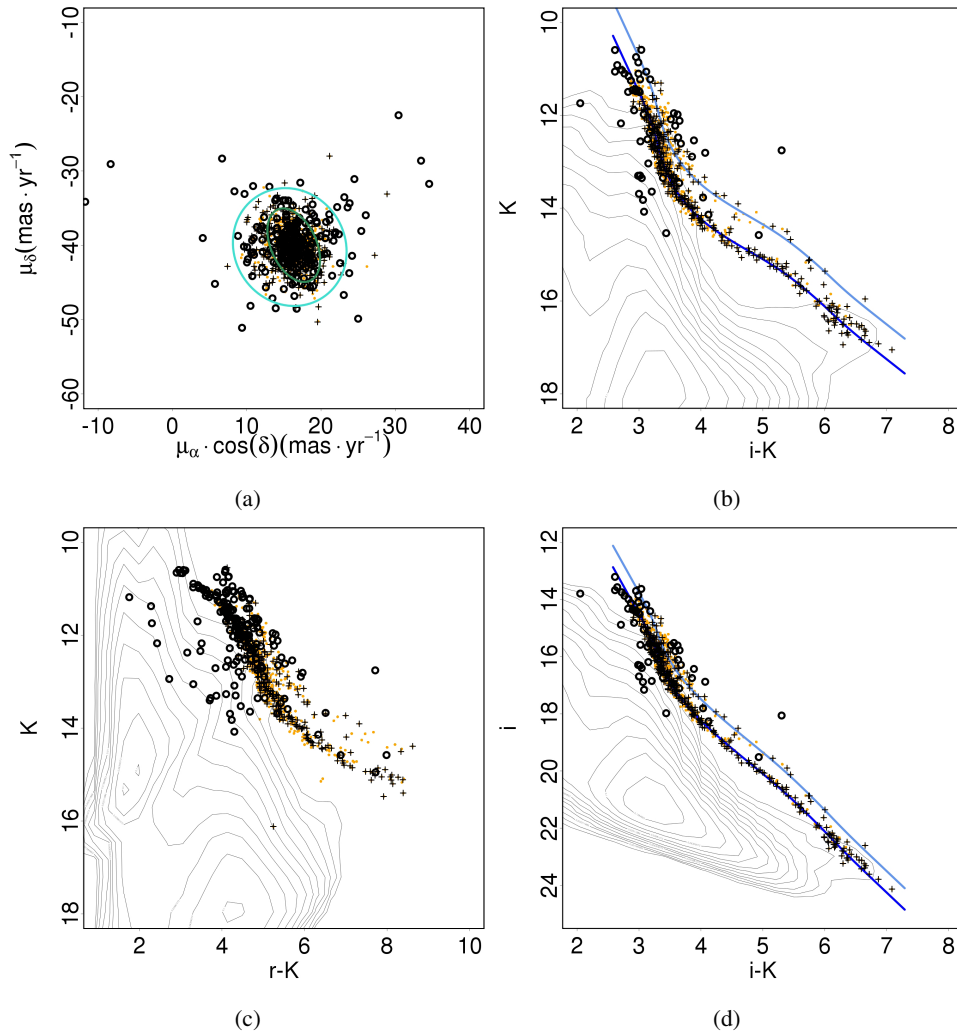


Fig. 3. Distribution of the sources that define the combined curvilinear and Gaussian likelihood model (the final reference set after all EM iterations) in the same 2D projections used in Fig. 1 (the VPD, and the $(i-K)-K$, $(r-K)-K$, and $(i-K)-i$ CMDs). Black circles represent sources in the initial reference set that were removed during the EM iterations, and black crosses represent complete sources added in the iterative process. Orange dots represent sources in both the initial and final reference sets.

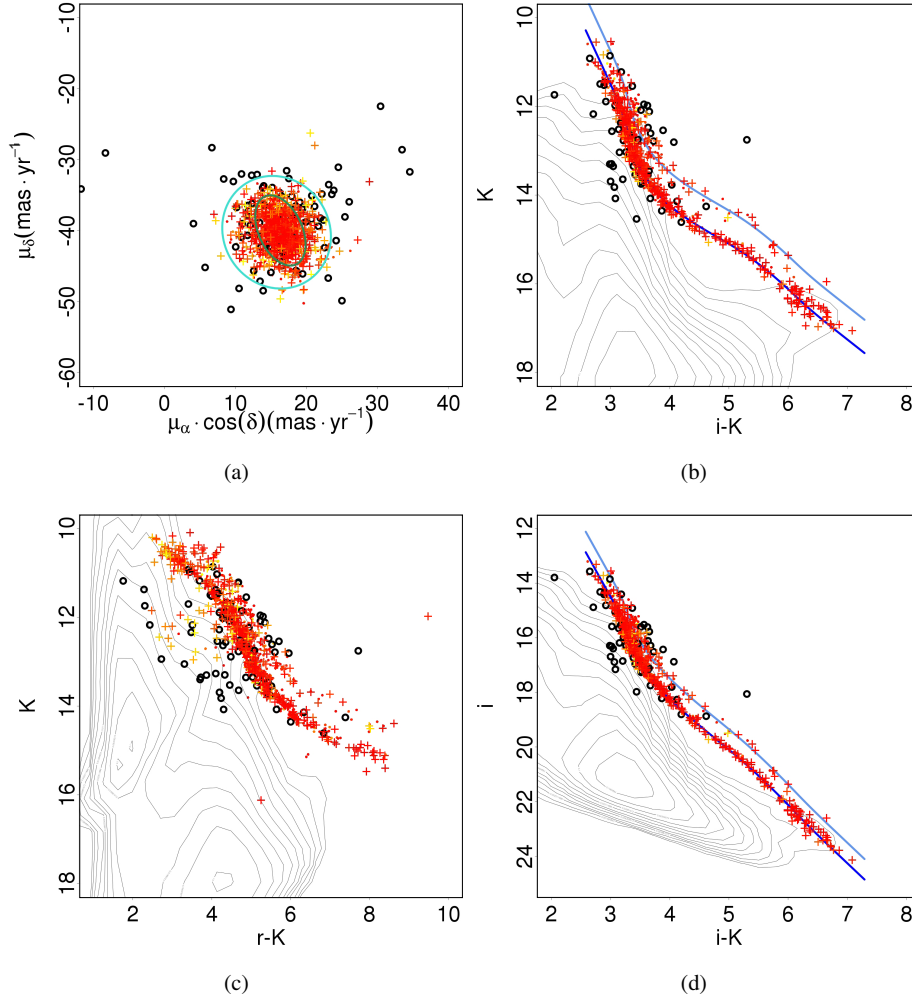


Fig. 4. DANCe catalogue sources (both complete and incomplete) with a membership probability above 0.975. Small dots represent sources in the original definition list; crosses represent member candidates not in the original definition list; black circles represent sources in the initial reference set with final membership probabilities below $p_{\min} = 0.975$. Contour lines trace the kernel density estimate obtained from the full data set. The colour code represents membership probability in a linear scale from yellow ($p = 0.975$) to red ($p = 1$).

obtained from the entire data set. Figure 3a shows the proper motion diagram, while Figs. 3b–d show the projections onto three CMDs. The coloured ellipses in Fig. 3a correspond to the $1-\Sigma$ level of the two Gaussian components in the proper motion subspace, obtained as a result of the methodology described in the previous sections. The fractional proportions of sources in each of these two Gaussian components are $\pi_{2,1} = 0.62$ (turquoise) and $\pi_{2,2} = 0.38$ (green). Sources included in the reference or training set during the last phase of iterations (with missing r magnitudes) do not appear in panel 3c. The contour lines in Fig. 3c show a clear bimodality, produced by the combination in the DANCe data set of two surveys with very different sensitivities.

The final number of sources in the set that defines the model components is 886, of which 531 were in the initial reference set from Stauffer et al. (2007). The remaining 355 new sources are marked with crosses in the various 2D projections in Fig. 3. On the other hand, 222 members in the initial membership list, were removed because of incompleteness, or during the EM iterations. These are marked with empty circles. In general, we see that the overall membership distribution in the scatter plots is maintained with respect to the initial reference set, except for the bright end of the K –($r - K$) sequence, where the lack of complete observations is the cause of the truncation. As we show in the next

section, this has a limited impact on the final list of members for the full data set. Apart from these incomplete sources, only some of the most conspicuous outliers are discarded after the EM iterations.

The last stage of iterations in the reduced space (with the r magnitude removed from the representation space) allows for a definition set that reaches fainter magnitudes ($i = 24$), illustrating the importance and advantages of having homogeneous coverage and sensitivity over the entire area of a survey.

4.1. Membership probabilities for sources with missing measurements

We subsequently use Eq. (10) to derive membership probabilities for sources with missing measurements in the RF-2 representation space. We define in general the list of cluster members as the set of sources with membership probabilities above p_{\min} (not to be confused with p_{in} , the probability threshold to include a complete source in the definition set).

Figure 4 shows the proper motion (4a) and CMDs (4a) for K versus $i - K$, 4a for K versus $r - K$, and 4d for i versus $i - K$ of the candidate member list for $p_{\min} = 0.975$. As in previous plots, crosses represent sources with membership probabilities higher than p_{\min} not in the initial reference set (thus, new members),

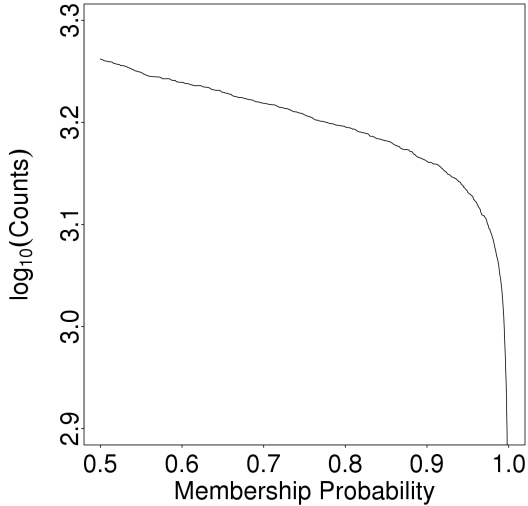


Fig. 5. Cumulative number of sources (on a logarithmic scale) in the DANCe catalogue with membership probabilities (inferred with the principal-curve model and $p_{\text{in}} = 0.975$, in the RF-2 representation space) above a given threshold.

black circles represent sources in the initial reference set with membership probabilities below p_{min} , and the membership probability is represented with a linear colour scale between yellow ($p = 0.975$) and red ($p = 1.0$).

For a membership threshold $p_{\text{min}} = 0.975$ the resulting list of members includes 652 of the 757 sources in the original membership list from the literature, and 604 new sources marked as plus signs in Fig. 4. For a somewhat more restrictive threshold $p_{\text{min}} = 0.9975$, the membership list contains 479 sources in the reference definition set, and 349 new members.

It is evident from Fig. 4a that the lack of constraints in the r magnitude results in a much more crowded K versus $r - K$ scatter plot, including a few clear outliers. Figure 5 represents the cumulative number of sources in the DANCe catalogue with membership probabilities above a given threshold.

Although not shown here for the sake of conciseness, the colour–magnitude distributions obtained with a mixture-of-Gaussians model for the entire representation space are remarkably similar in shape to the results of the combined mixture-of-Gaussians plus principal-curve model.

4.2. Performance assessment with synthetic samples

The probabilistic models (likelihoods) obtained from the EM iterations can be used to generate artificial samples of sources, and the method described in Sect. 2 can then be applied to the synthetic data set to determine whether it can recover the input set of members, and assess the contamination level as a function of the threshold adopted to define the membership. The validity of these assessments will in turn depend on the validity of the inferred likelihoods.

We generated five samples of two million sources each, with the same proportion of members as derived from the analysis of the DANCe data set. Initially, the two million sources in each sample are generated without missing values, and then some of the magnitudes were masked as not available following the frequencies determined from the DANCe data set. Finally, we assigned to each source in the synthetic catalogue the measurement uncertainties of the closest (in the Euclidean sense) DANCe

source with the same pattern of missing variables. This means that in the ideal case, we would have generated a new sample of sources from the same probability distribution that generated the DANCe data set. Of course, this would only be true if the model inferred from the DANCe data set was exactly the probability distribution that generated it.

Table 4 summarises the evaluation of our algorithm on the synthetic data set, expressed in terms of two quantities: the true positive rate (TPR, the fraction of real members recovered by the algorithm) and the contamination rate (CR, the fraction of the list of member candidates drawn from the field density distribution). Each quantity is accompanied by an estimate of the uncertainty derived from the range of values observed in the five samples drawn from the distribution. The uncertainty is defined as the radius of that interval.

The ideal outcome of the experiment would be a classifier that obtained a 100% TPR without contamination. In that respect, the point closest to this optimum in the curve defined by the varying membership thresholds corresponds to $p = 0.85$, TPR = 92.9% and CR = 4.5%. We nevertheless considered that the optimum along the curve cannot be defined uniquely because it is context dependent: some research projects will demand very low contamination rates regardless of the membership list completeness, while others will have opposite requirements. We therefore opted for providing the full list of posterior probabilities and let the catalogue user define his/her membership threshold.

5. Sensitivity analysis

In this section we analyse the dependence of the set of members obtained on three particular choices: the probability threshold to include a source in the set that defines the model (p_{in}), the representation space, and the probability threshold for inclusion in the set of cluster members (p_{min}).

Table 5 summarises the number of sources used to define the model in the principal curves framework, for three representation spaces (RF-2, RF-3 and the set of apparent magnitudes) and admission probability thresholds ($p_{\text{in}} = 0.9545, 0.975$ and 0.9975). The first three columns contain the definition set sizes at the end of the last set of iterations (those in the reduced space, without r related features) while the rightmost three columns show the number of sources in the entire DANCe data set (comprising complete and incomplete sources) with membership probabilities above 0.75 and 0.9975. When comparing the left and right numbers in Table 5, it has to be kept in mind that members in the reference set are only removed from it in subsequent iterations if their membership probabilities fall below 0.5. According to Table 5, a tendency for smaller definition set sizes is to be expected from higher admission thresholds, but the influence of these changes on the final membership lists sizes is far from straightforward.

Figure 6 shows the distribution of sources (complete or incomplete) with probabilities above 0.9975, after the projection onto the reduced space (thus removing the r magnitude) in the proper motion (bottom row) and $i - (i - K)$ (top row) diagrams. The cluster sequences in the $i - (i - K)$ diagrams correspond, from left to right, to the AM, RF-2, and RF-3 feature sets. The latter two are displaced in the x -axis by one and two units, respectively, for the sake of clarity. The colour code reflects the membership probability on a linear scale, from yellow ($p = 0.9975$) to red ($p = 1$). The VPDs in the bottom row show AM candidates as black points, RF-2 candidates as green points, and RF-3 candidates as orange points. The three feature spaces convey

Table 4. True positive rates and contamination rates for different values of the membership threshold.

p_{\min}	0.50	0.7	0.8	0.90	0.95	0.96	0.97	0.98	0.99	0.9975
TPR (%)	98.4 ± 0.5	97.1 ± 0.7	96.0 ± 0.9	92.9 ± 1.5	88.0 ± 2.8	85.9 ± 3.0	82.6 ± 3.2	76.7 ± 4.9	63.8 ± 7.7	36.3 ± 7.7
CR (%)	11.0 ± 2.0	8.0 ± 1.5	6.6 ± 1.3	4.5 ± 1.1	2.9 ± 0.5	2.6 ± 0.6	2.1 ± 0.5	1.6 ± 0.3	1.1 ± 0.3	0.4 ± 0.4

Notes. The uncertainty intervals correspond to the range of values (maximum–minimum) observed in the five random samples.

Table 5. Number of members in the final converged reference set (left) and in the DANCe catalogue (right).

Admission threshold	Definition set			DANCe catalogue		
	RF-2	RF-3	AM	RF-2	RF-3	AM
$p_{\text{in}} = 0.9545 (2\sigma)$	911	882	910	1690:930	1543:916	1578:1014
$p_{\text{in}} = 0.975 (2.2\sigma)$	886	881	896	1612:828	1556:979	1567:1032
$p_{\text{in}} = 0.9975 (3\sigma)$	827	810	827	1565:829	1474:769	1575:977

Notes. The sizes of the definition set correspond to the final sets after convergence of all EM iterations. The number of members in the DANCe catalogue is listed for membership probabilities higher than 0.75 and 0.9975 (separated by a colon). In both cases, the sizes are listed for three representation spaces (all magnitudes, RF-2, and RF-3) and probability thresholds (0.9545, 0.975, and 0.9975).

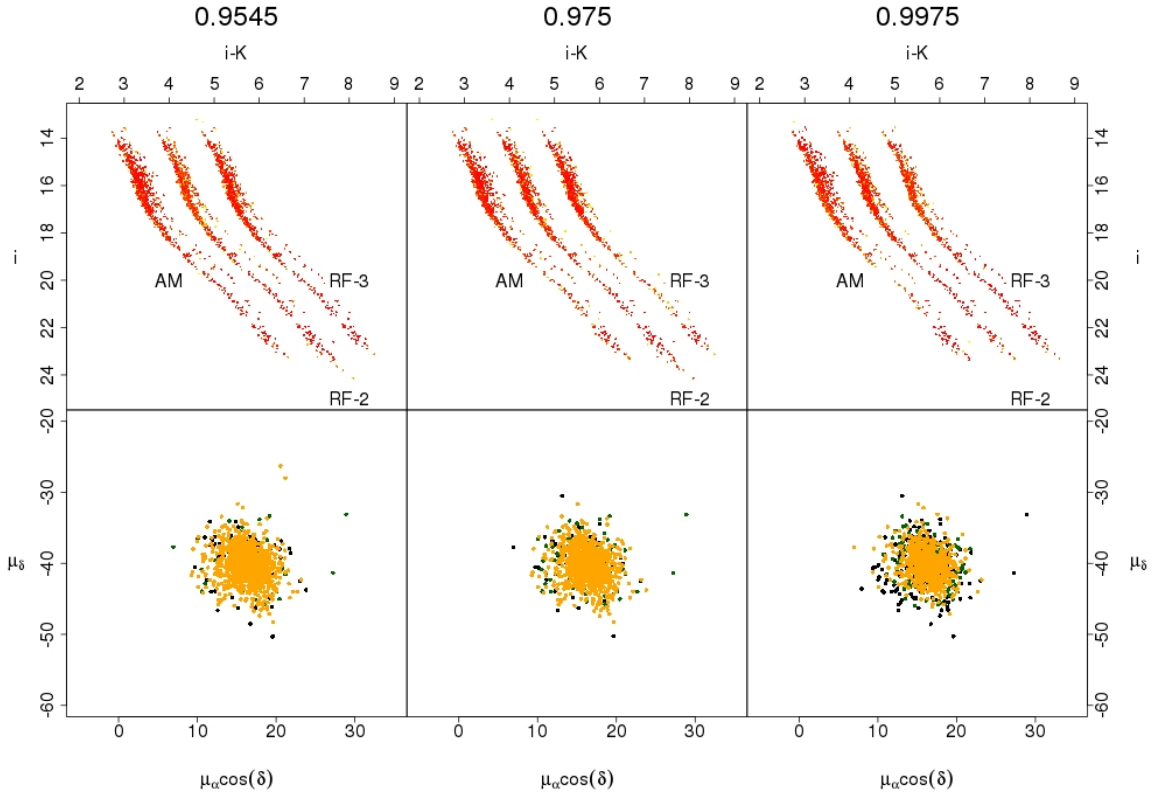


Fig. 6. Vector point diagrams (*bottom row*) and $(i - K)$ - i CMDs (*top row*) of sources in the DANCe catalogue (both complete and incomplete) with membership probabilities above 0.9975, for three values of the admission threshold p_{in} to the definition set (0.9545 in the *left column*, 0.975 in the *middle column*, and 0.9975 in the *right column*). Each CMD shows the three cluster sequences obtained with the AM (*left*), RF-2 (*middle*), and RF-3 (*right*) representation spaces. The colour code in the top row reflects the membership probability in a linear scale from yellow ($p = 0.9975$) to red ($p = 1$). In the VPD diagrams, we use black, green, and orange points to represent candidates obtained in the AM, RF-2, and RF-3 representation spaces.

very similar cluster sequences except for a larger scatter in the brighter segment of the AM feature set, and a sequence reaching fainter sources in the RF-2 space with $p_{\text{in}} = 0.9545, 0.975$.

Figure 7 shows the cumulative number of sources (on a logarithmic scale) with membership probabilities above a given value. Continuous lines correspond to the 2σ definition set (black for RF-2, orange for RF-3, and blue for the AM feature

set); long-dashed lines correspond to the 2.2σ threshold, and short-dashed lines correspond to the 3σ threshold (with the same colour code in the three thresholds). We see that although all feature sets result in relatively stable membership probabilities, the AM set results are less affected by changes in the threshold for inclusion in the reference set, especially as the membership threshold is reduced. It also shows that more

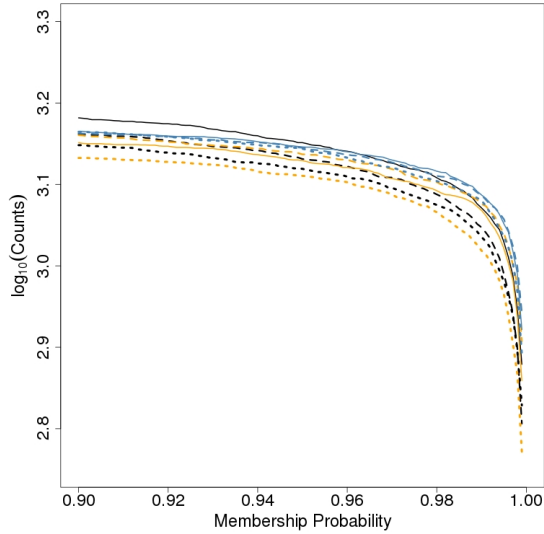


Fig. 7. Cumulative number of sources in the DANCe catalogue with membership probabilities above a given value for the AM (blue), RF-2 (black), and RF-3 (orange) feature sets. Continuous lines represent models derived with $p_{\text{in}} = 2\sigma$, long-dashed lines correspond to $p_{\text{in}} = 2.2\sigma$, and short-dashed lines to $p_{\text{in}} = 3\sigma$.

restrictive admission thresholds p_{in} result in shorter membership lists for a fixed probability, except in the RF-2 space. In general, the relationship for a given feature set between the p_{in} threshold and the final membership probabilities is not always straightforward. The intuition that a higher threshold p_{in} should result in lower membership probabilities for the full data set does not always apply. This is because the set of sources used for the model definition (that is, the set of sources with measurements in the full set of features, referred to in this work as complete sources) does not necessarily follow the same probability density in the feature space as the full data set (including the incomplete sources). Thus, a higher threshold may result in changes in the d -dimensional model (2D Gaussian mixture plus the principal curve) such that the new model passes through regions with a higher or lower density of incomplete sources, or both, in different curve segments. This problem would be solved if we used all sources (complete and incomplete) to define the cluster probabilistic model, as indicated in Sect. 6.

Figure 8 shows the membership probabilities in the three representation spaces (AM, RF-2, and RF-3, from left to right) obtained with two admission thresholds corresponding to 2- and 3 σ detections (x - and y -axes, respectively). The colour code reflects the apparent i -band magnitude on a linear scale and shows no systematic effect for points away from the diagonal. We see that the AM scatter plot portrays a significant lack of robustness, with a large proportion of sources changing the membership probability significantly. The RF-2 and RF-3 representation spaces, in contrast, show a reasonable stability in the membership probabilities assigned, with the RF-2 showing a more stable behaviour in the region of $p = 1$.

Figure 9 shows the correlation between the membership probabilities obtained in the RF-2 and RF-3 representation spaces for the three values of p_{in} tested in the experiments. The colour scale represents the i -band magnitude on a linear scale from black ($i \approx 13$) to red ($i \approx 25$) and shows no systematic trend for the deviations from the diagonal. We find evidence of membership probabilities obtained in the two representation spaces that strongly disagree. This is to be expected because a source

can be in a region of high probability density in the variables of one representation space, but be an outlier in a subspace of the other, especially if the source has not been observed in a large part of the common feature space (that is, in the subspace of features common to RF-2 and RF-3), or if some photometric measurements are problematic (e.g. affected by cosmic rays or bad pixels) in the set of magnitudes specific to a feature space. But these are not a large or significant portion of the total.

From Figs. 7–9 it is evident that the various approaches convey slightly different membership lists. This is an problem that is usually not dealt with in the literature: the fact that any membership analysis depends (amongst other factors) on the representation space used and on the membership threshold adopted. Because we are aware that from a scientific perspective, different objectives require different samples, we provide a series of catalogues, one for each experiment described. This way, the reader can decide which experimental setup best suits his/her needs. It must be kept in mind that any particular choice will always be a compromise between contamination (which may increase with decreasing membership probability thresholds) and completeness (reduced if very strict criteria are adopted). However, the relative stability of the RF-2 membership probabilities with increasing admission threshold, and the better coverage of faint sources visible in Fig. 6 two desirable properties that make it a better choice than the other two feature sets. Neither the reference set defining the likelihood model, nor the distribution of final membership probabilities obtained with this feature set change much with the admission threshold p_{in} , and thus, we do not recommend a particular set of probabilities. Figure 9 shows that the high-probability sources are the same in the two representation spaces, except for a few sources. These discrepancies can be explained by the fact that RF-3 includes one magnitude that is not present in RF-2: the Z-band magnitude. This implies that a source with a high membership probability in the RF-2 representation space, but with a Z-band magnitude that places it at a large Mahalanobis distance from the principal curve, can have a significantly lower membership probability in the RF-3 space.

Finally, we briefly analyse the sensitivity of the membership lists with respect to the ad hoc choice of proportions (80/20) for the parallel sequence of equal-mass binaries. We checked post-hoc the proportion of sources with higher probability to belong to this parallel sequence. We did this for complete sources in the final definition set of the RF-2 representation space and a p_{in} threshold equal to 0.975. Given the final principal-curve model for the likelihood in the CM subspace and its parallel replicate 0.75 mag above, we computed for each source in the definition set the probability that each of the two parallel sequences generated the source, taking into account the measurement uncertainties. We assumed that the source was generated by the sequence that produces the higher probability. The resulting proportion of 82.2/17.8 agrees reasonably well with the input priors. The methodology is fairly robust because the proper motion measurements strongly constrain the CM subspace model. As a final check of the robustness of our results, we ran exactly the same model (in the RF-2 representation space and with the same p_{in} probability threshold for admission of members to the definition set) with a 50/50 prior probability for the two sequences. The resulting definition set was qualitatively and quantitatively identical except for one source in the 80/20 set that is missing from the 50/50 set. As a consequence, the principal-curve likelihood model is indistinguishable in the two cases, and so are the resulting membership probabilities for the incomplete

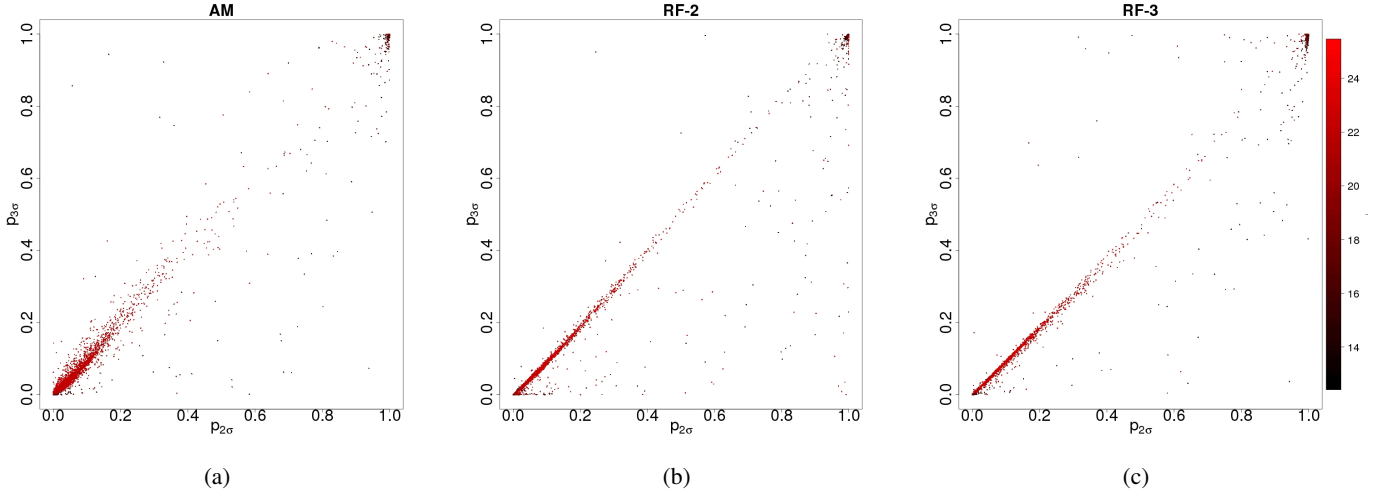


Fig. 8. Scatter plots of the membership probabilities for the AM (*left*), RF-2 (*middle*), and RF-3 (*right*) feature sets, and for two values of the admission probability threshold p_{in} , namely 0.9545 (2σ detection, x -axis) and 0.9975 (3σ detection, y -axis). The colour code reflects the apparent i -band magnitude according to the colour scale to the right.

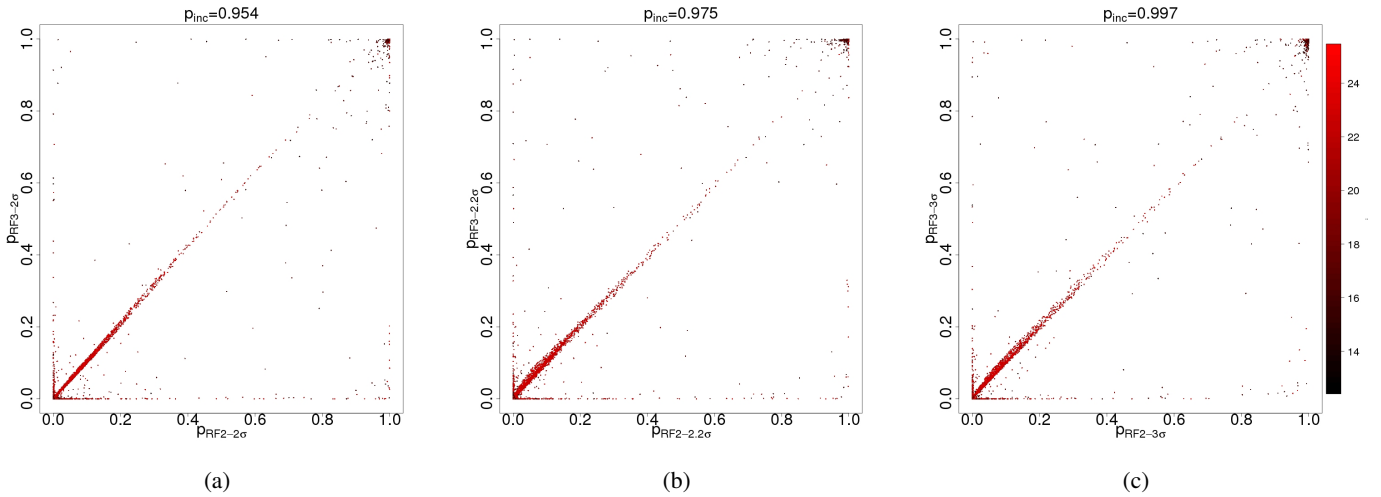


Fig. 9. Scatter plots of the membership probabilities for the RF-2 versus RF-3 representation spaces for three values of the admission probability threshold $p_{\text{in}} = 0.9545$ (2σ detection, *left*), 0.975 (2.2σ detection, *middle*), and 0.9975 (3σ detection, *right*). The colour code reflects the apparent i -band magnitude according to the colour scale to the right.

sources, rendering the results virtually independent (to within reasonable limits) of the choice of this prior proportion.

6. Method limitations and conclusions

We extended the classical procedure to infer membership probabilities to deal with proper motions and multiband photometry on an equal basis and consistently across the full magnitude range. We constructed a maximum-likelihood, unique multidimensional probabilistic model using the EM algorithm and an initial reference set of sources assumed to be cluster members.

There are, however, a few caveats and limitations that must be made clear to understand how the membership probabilities can be used in future studies.

In the first place, we did not include incomplete sources in the derivation of the likelihood models. This is a valuable source of information that can be incorporated in a consistent derivation of the model parameters from the complete data set.

We also incorporated the measurement uncertainties in the inference of the source membership probability (as described

in Eq. (8)), but we did not include them in the derivation of the probabilistic models. In fact, the covariance matrix used for any given value of λ (the parameter along the principal curve), was calculated from the set of sources that project to that value of λ , and thus is an overestimate of the true isochrone width, as explained in Sect. 2.4. Had we included the measurement uncertainties in the derivation of the likelihood model, the resulting covariance matrices in $p(m_{\text{CM}}|\lambda)$ would have been narrower and the membership probability estimates lower for sources far from the isochrone.

Furthermore, we did not infer the binarity fraction in the principal-curves model for the photometric subspace. We fixed values ab initio that were assumed to be constant all along the sequence, which does not apply in reality, as shown in Figs. 3 and 4. Nor did we explicitly model the contribution of unequal mass binaries to the probability density of sources in the representation space (although these systems are recovered as members due to the overestimation of the covariance of the models).

Finally, we have no estimate of the uncertainties in the inferred membership probabilities themselves, a direct

consequence of using a maximum-likelihood model. Neither have we uncertainties on derived distributions such as the density of sources along the principal curve (a proxy to the IMF). We are currently working on the construction of a hierarchical model (see e.g. Gelman & Hill 2007; Hogg et al. 2010, and references therein for applications in the field of astrophysics) from the DANCe data set for the Pleiades and other young stellar clusters. In this framework of multilevel or hierarchical models, the observations (proper motions and multiband photometry in our case, but this can be generalised to any kind of data) are treated as outcomes drawn from probabilistic distributions, the parameters of which are, in turn, drawn from higher-level probability distributions (which include the IMF, or the star formation rate and the IMF if stellar evolution models are assumed). The parameters of these higher-level distributions are known as hyperparameters. In our case (and just as an illustrative example of the power of these models), instead of using a maximum-likelihood estimate of the probability density of sources along the principal curve, we parameterise the density along the curve, and include these new parameters into the set to be inferred from the data. This way, we can derive a posterior-probability distribution for the biased and censored luminosity function (LF) and obtain uncertainty estimates or confidence intervals for its value at a given position along the sequence. This can be achieved by propagating the measurement uncertainties in a consistent way, upwards along the various levels of the hierarchy. Of course, to take full advantage of the power of hierarchical models, we can go beyond the observed, biased and censored LF and try to infer the unbiased, uncensored LF up to the highest observed luminosity (beyond that point, and due to the lack of observational constraints, the uncertainties on the model parameters increase). This, however, comes at the cost of modelling the observational biases, and potentially complex and poorly known distributions such as that of the reddening or the 3D spatial density of sources.

In future articles of this series we will analyse the consequences of the membership probabilities derived here on the distributions of properties of the Pleiades sources and compare these distributions with previous studies of the cluster.

Acknowledgements. H. Bouy is funded by the Ramón y Cajal fellowship program number RYC-2009-04497. H. Bouy acknowledges funding and support of the Université Joseph Fourier 1, Grenoble, France. This research has been funded by Spanish grants AYA2012-38897-C02-01, AyA2011-24052, AYA2010-21161-C02-02, CDS2006-00070 and PRICIT-S2009/ESP-1496. E. Moraux acknowledges funding from the Agence Nationale pour la Recherche program ANR 2010 JCJC 0501 1 “DESC (Dynamical Evolution of Stellar Clusters)”. J. Bouvier acknowledges funding from the Agence Nationale pour la Recherche program ANR 2011 Blanc SIMI 5-6 020 01 (“Toupiés”). J. Bouvier and E. Moraux acknowledge support from the Faculty of the European Space Astronomy Centre (ESAC). E. Bertin acknowledges partial funding of computer resources by the French Programme National de Cosmologie et Galaxies and CNRS-Fermilab contract #367561. This work has made an extensive use of Topcat (<http://www.star.bristol.ac.uk/~mbt/topcat/>, Taylor 2005).

References

- Balaguer-Núñez, L., Galadí-Enríquez, D., & Jordi, C. 2007, *A&A*, 470, 585
 Boudreault, S., Lodieu, N., Deacon, N. R., & Hambly, N. C. 2012, *MNRAS*, 426, 3419
 Bouy, H., Bertin, E., Moraux, E., et al. 2013, *A&A*, 554, A101
 Breiman, L. 2001, *Machine Learning*, 45, 5
 Deacon, N. R., & Hambly, N. C. 2004, *A&A*, 416, 125
 Gelman, A., & Hill, J. 2007, *Data Analysis Using Regression and Multilevel/Hierarchical Models*, Analytical Methods for Social Research (Cambridge University Press)
 Hastie, T., & Stuetzle, W. 1989, *J. Am. Stat. Assoc.*, 84, 502
 Hastie, T., & Tibshirani, R. 1990, *Generalized Additive Models*, Monographs on statistics and applied probability (Chapman & Hall, CRC Press)
 Hogg, D. W., Myers, A. D., & Bovy, J. 2010, *ApJ*, 725, 2166
 Kozhurina-Platais, V., Girard, T. M., Platais, I., et al. 1995, *AJ*, 109, 672
 Krone-Martins, A., & Moitinho, A. 2014, *A&A*, 561, A57
 Lodieu, N. 2013, *MNRAS*, 431, 3222
 Lodieu, N., Deacon, N. R., & Hambly, N. C. 2012a, *MNRAS*, 422, 1495
 Lodieu, N., Deacon, N. R., Hambly, N. C., & Boudreault, S. 2012b, *MNRAS*, 426, 3403
 Malo, L., Doyon, R., Lafrenière, D., et al. 2013, *ApJ*, 762, 88
 Murphy, K. P. 2012, *Machine Learning: A Probabilistic Perspective (Adaptive Computation and Machine Learning series)* (The MIT Press)
 Platais, I. 1991, *A&AS*, 87, 69
 Sanders, W. L. 1971, *A&A*, 14, 226
 Schwarz, G. 1978, *Ann. Statist.*, 6, 461
 Stauffer, J. R., Hartmann, L. W., Fazio, G. G., et al. 2007, *ApJS*, 172, 663
 Taylor, M. B. 2005, in *Astronomical Data Analysis Software and Systems XIV*, eds. P. Shopbell, M. Britton, & R. Ebert, ASP Conf. Ser., 347, 29
 Vasilevskis, S., Klemola, A., & Preston, G. 1958, *AJ*, 63, 387